2017 International Symposium on Nonlinear Theory and Its Applications,
NOLTA2017, Cancun, Mexico, December 4-7, 2017

Implementation of Both Synapse and Neuron on a Field-Induced Insulator-to-2D Metal Transition Device with $SrTiO_3$ Channel.

Pablo Stoliar[†,‡], Alejandro Schulman[†], Ai Kitoh[†], and Isao H. Inoue[†]

†National Institute of Advanced Industrial Science and Technology (AIST)
AIST Central 5, 1–1–1 Higashi, Tsukuba 305-8565, Japan
‡CIC nanoGUNE
Tolosa Hiribidea 76, 20018 Donostia–San Sebastian, Spain
Email: p.stoliar@aist.go.jp, isaocaius@gmail.com

Abstract—Surfaces of $SrTiO_3$ (STO) are widely known as a playground of basic physical researches of two-dimensional metallic systems. By electrostatic carrier-density modulation of the STO surface, a variety of interesting phenomena such as an insulator to 2D metal transition (IMT), superconductivity, and ferromagnetism are triggered. Here we demonstrate a unique challenge; neuromorphic electronic devices are implemented on the electrostatic control of the IMT at the STO surface. We prove that our STO device is indeed a promising candidate of an artificial neuron (leaky-integrate and fire: LIF) as well as an artificial synapse (spike-timing-dependent plasticity: STDP). This work will bridge the gap between the basic research of IMT and its viable applications.

1. Introduction

Miniaturisation limit has been a looming crisis of the semiconductor industry for decades, and is now a pressing issue to be averted. A near-future nanometre-sized semiconductor device contains only a few dopants, so that we can no more distinguish on/off states from the thermal noise. One of the promising ideas to overcome the crisis is to utilise the electrostatic control of insulator to 2D metal transition (IMT), because the 2D metal contains a large number of carriers ($\gtrsim 10^{13}$ cm^{-2}), ensuring the scalability far beyond the crisis. Our challenge is to develop future electronics based on such kinds of IMTs observed in any "post-Si" materials with a variety of concomitant functionalities. However, those "post-Si" materials with IMTs have intrinsic defect-prone surfaces in general; especially, oxygen vacancies are easily created.

In this report, we show how to turn the lemon into lemonade; *i.e.*, we turn the migration of oxygen vacancies in the well-known post-Si material $SrTiO_3$ (STO) into a proactive tool to control its IMT. By sweeping out the intrinsic oxygen vacancies in STO using the external electric field without creating further extrinsic oxygen vacancies at the surface, a polar region is created near the surface. The polarity of the region behaves as an effective back-gate and induces more carriers at the surface than those simply induced by the external field. Then, the IMT is driven at the surface. Simultaneously, the Thomas-Fermi screening sets in, and the screening length for the external field is shortened drastically. This results in a large but well-controlled hysteresis in the current-voltage relation, which is quite advantageous for implementing an artificial synapse on this device. Moreover, the dynamics of IMT give rise to another functionality; the threshold voltage of IMT is changed by an accumulation of input pulses applied to the device. This indicates our device can work as an artificial leaky-integrate-and-fire (LIF) neuron, which does not require the external and voluminous LI part. We discuss here those neuromorphic applications of IMT in the light of possible physical mechanisms.

2. FET Device Utilising IMT of STO

We have fabricated an accumulation-mode field-effect transistor (FET) on a highly insulating undoped single-crystalline STO. A Parylene-C (6 nm) / HfO_2 (20 nm) double layer was utilised as a gate insulator [1] (Fig. 1(a)), where the Parylene-C layer works to protect the STO

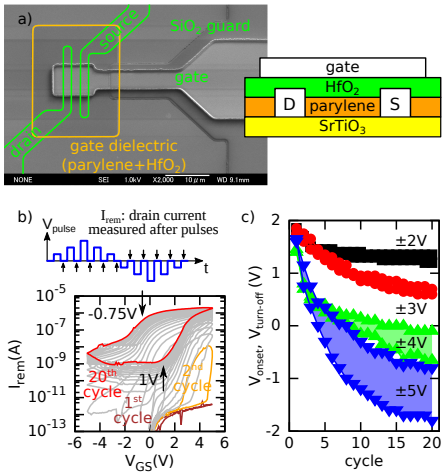

Figure 1: a) SEM image of our STO FET and a schematic picture of the cross section. b) Remnant drain current I_{rem} plotted against V_{GS} (bottom), but each data point of I_{rem} was measured after each V_{GS} pulse was applied (top). c) Evolution of the onset and turn-off voltages of the hysteresis in the I_{rem}-V_{GS} plot for different V_{GS} sweep ranges.

surface from extrinsic oxygen-defect formations during the device fabrication process as well as during the gate electric-field application.

Our STO FET has three qualitatively different conduction regions. The sub-threshold region is below the threshold voltage $V_{\rm th} \approx 1.8\,$V, where our STO FET shows fairly small subthreshold swing (170 mV/decade) that is much smaller than the values ever reported for STO FET [2]. Above $V_{\rm th}$ is the so-called accumulation region. However, the channel becomes metallic above $V_{\rm IMT} \approx 3.5\,$V due to the IMT [3, 4], and the evolution of the channel is well explained by a percolation model [2, 4, 5, 6] with the IMT boundary of Mott-Ioffe-Regel limit h/e^2, indicating the metallic state is two dimensional (2D) [3, 4]. The 2D metallic state holds a large sheet carrier density ($\gtrsim 10^{14}\,$cm^{-2}) and high mobility ($\gtrsim 10\,$cm^2/Vs) [2].

3. Hysteresis due to IMT

A substantial hysteresis appears for $V_{\rm GS} \gtrsim V_{\rm IMT}$ as shown in Fig. 1(b). The plot is called hysteresis switching loop (HSL) [7] and was obtained as follows. We applied rectangular-shaped $V_{\rm GS}$ pulses with the amplitude $V_{\rm pulse}$, the width of 0.75 s, and the period of 1.6 s (blue lines in Fig. 1(b) top). $V_{\rm DS} = 0.1$V was constant. We measured $I_{\rm D}$ while $V_{\rm GS}$ pulse is off (at the time indicated by black arrows in Fig. 1(b) top). This $I_{\rm D}$ is called remnant current $I_{\rm rem}$. Each $I_{\rm rem}$ was plotted against $V_{\rm GS}$, which is in fact the value of $V_{\rm pulse}$ just before each $I_{\rm rem}$ was measured.

$V_{\rm GS}$, *i.e.*, $V_{\rm pulse}$, is swept in cycle between minimum and maximum values. As the cycle progresses, the system converges to a stable state (Fig. 1(c)). This means the first 20 cycles can be regarded as "electroforming" for obtaining the stable HSL. In the stable HSL, the remnant channel conductance is modulated between 10 μS and 10 nS with the threshold voltages of $V_{\rm pulse} \approx 1\,$V and $V_{\rm pulse} \approx -0.75\,$V.

The hysteresis is understood by a migration of oxygen-vacancies (V_o) in the bulk of STO near the channel surface (Fig. 2). Initially, the channel is highly insulating with only a small amount of intrinsic oxygen vacancies originated in possible surface reconstructions and bulk dislocations. When a positive $V_{\rm GS}$ is applied, $V_o \rightarrow e^- + V_o^+$ occurs, where e^- is an electron and V_o^+ is the positively charged oxygen vacancy. (To be exact, oxygen vacancy is divalent. In Kröger-Vink Notation, it is $V_o^{\times\times} \rightarrow 2e' + V_o^{\bullet\bullet}$. But for simplicity we use V_o^+ here instead of $V_o^{\bullet\bullet}$.)

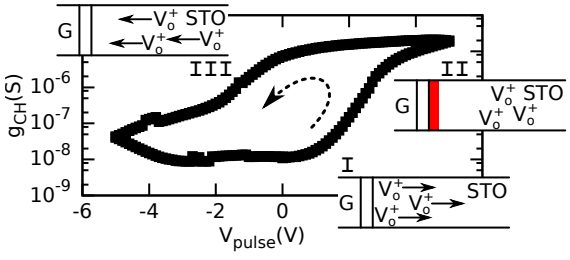

Figure 2: Schematic description of the effect of the V_o^+ migration for the stable HSL. Scene **I**: V_o^+ drifts towards the bulk due to the gate electric field. Scene **II**: for $V_{\rm GS}$ above $V_{\rm IMT}$, the electric drift of V_o^+ is interrupted by the Thomas-Fermi screening of the 2D metallic state (red). Scene **III**: for negative $V_{\rm GS}$, the V_o^+ drifts back towards the interface.

As schematically shown in the scene **I** of Fig. 2, V_o^+ is repelled towards the bulk of STO due to the positive $V_{\rm GS}$ field penetrating in the bulk of STO, whereas e^- is accumulated in the channel. The drift of V_o^+ generates a defect-free region in the bulk of STO, which is called a migration-induced field-stabilized polar (MFP) region [8] that maintains its polarity by a displacement of the Ti ion. This polarity of the MFP region acts as a virtual but quite effective back-gate, which works to decrease the threshold voltage. When $V_{\rm GS}$ reaches $V_{\rm IMT}$, the IMT is triggered at the surface of STO, resulting in a complete screening of the gate electric field (Thomas-Fermi screening). Then the electric drift of V_o^+ stops (scene **II**) and the significant hysteresis is induced. The sudden change of the screening length also causes a strong phase shift between $V_{\rm GS}$ and $I_{\rm D}$ as described below. Once the channel returns to be semiconducting by decreasing $V_{\rm GS}$, V_o^+ starts drifting towards the interface for negative $V_{\rm GS}$, closing the hysteresis cycle (scene **III**).

4. STDP Synapse

The hysteresis of the HSL curves is beneficial for neuromorphic applications. A well-established experiment [9] to evaluate the spike-timing-dependent plasticity (STDP) behaviour was applied to our STO FET to examine whether our STO FET works as an artificial synapse. Two dc voltages, $V_{\rm DS}$ and $V_{\rm bias}$, set the operating point of STO FET, and we applied pre- and post-pulses ($-V_{\rm pre}$ and $V_{\rm post}$) to the gate (Fig. 3(a)). The shapes of our pre- and post-pulses are same as those used in literature [9]. Although neither $V_{\rm pre}$ nor $V_{\rm post}$ has enough amplitude to change the channel conductance, when the time difference between post- and pre-pulses $|\Delta t| = |t_{\rm post} - t_{\rm pre}|$ is comparable or smaller than the pre- and post-pulse width τ, the two pulses overlap to each other, and the maximum amplitude of the composed pulse becomes larger than both $V_{\rm pre}$ and $V_{\rm post}$. Then, the channel conductance is modulated. This modulation as a function of Δt is called an STDP behaviour.

Our STO FET eventually showed an ideal STDP behaviour (Fig. 3(b)). Most of the single-device synapses under intensive studies nowadays utilise stochastic events such as a filament formation. Therefore, the STDP behaviours for those devices are intrinsically associated with the significant noise. On the contrary, the stability of the STDP characteristics of our device is surprisingly outstanding. To make it obvious, we fitted our STDP data to a tractable virtual STDP curve. Figure 3(c)–(e) exhibit the results, and the residues of the fitting are compared with those of a typical synapse based on a filament formation [10]. The standard deviation of our STO FET synapse

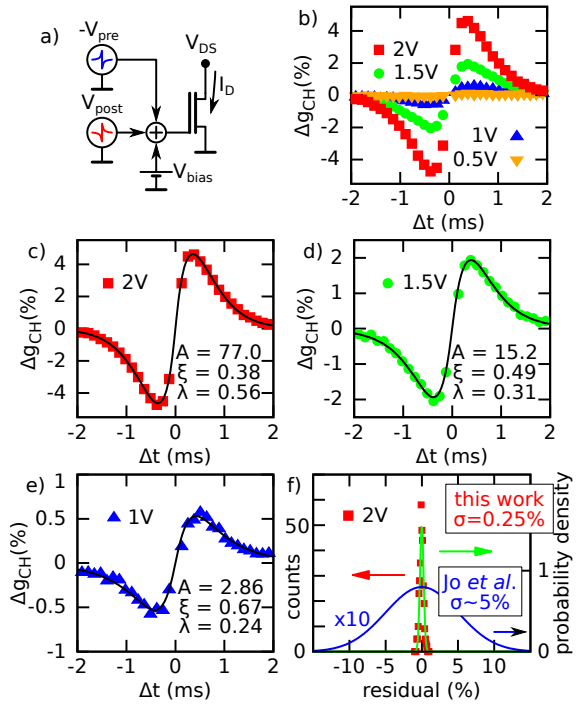

Figure 3: a) Setup of our STDP experiments with fixed V_{DS} of 0.1V. b) STDP curves for different pulse amplitudes. The modulation of the remnant channel conductance is plotted against the relative timing between pre- and post-pulses. c)–e) Fitting of the STDP curves with the phenomenological function $\Delta g_{CH} = A[1/\{\exp(-\Delta t/\xi)+1\}-0.5]\exp(-|x|/\lambda)$, where A, ξ, and λ, are fitting parameters. f) Fitting residuals for the data shown in (c) for ten independent experiments compared to those in literature [10]

is 20 times smaller.

We consider this is because we use IMT for our STDP behaviour. The number of carriers in the metallic channel of our STO FET is several orders larger than that of the standard electrostatic devices [4], which results in a large dynamic range (Fig. 1(b)), and alleviates the stochastic noise. This is a great advantage of our STO FET to be used for an artificial synapse.

5. LIF Neuron

The IMT of the FET channel has another interesting feature for neuromorphic applications. In any FETs, the gate electric field penetrates into the bulk of the channel. For semiconductor FET, the length scale corresponds to a classic Debye screening length. When the IMT occurs, the longer Debye screening length is replaced by the extremely short Thomas-Fermi screening length for metal. The dynamics cause the phase shift between V_{GS} and I_D as schematically shown in Fig. 4(a), where the screening length L_D (blue line) alternates between SC (Debye screening length for semiconducting channel) and T-F (Thomas-Fermi screening length for metallic channel) for the cyclic change of V_{GS}. The phase shift between the V_{GS} input and

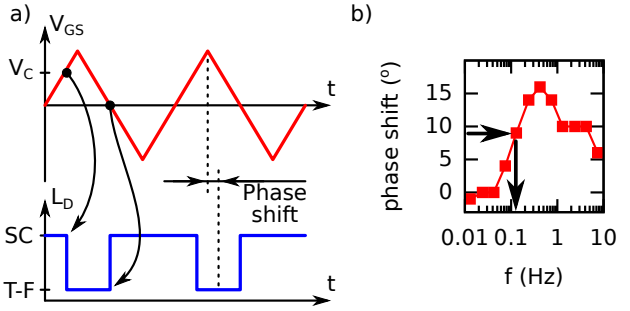

Figure 4: a) Schematic picture of the phase shift. See text for details. b) Experimental results. We applied a sinusoidal $V_{GS} = 2.8 + 0.05\sin(\omega t)$ to our STO FET biased with $V_{DS} = 0.1$ V, and measured the phase shift of $I_D(t)$.

the change of L_D is clearly seen there. This is because IMT occurs at $V_{GS} = V_{IMT}$ for increasing V_{GS}, but for decreasing V_{GS} it does not occur at $V_{GS} = V_{IMT}$. Fig. 4(b) shows our experimental results. We applied a sinusoidal $V_{GS}(t)$ and measured $I_D(t)$. The phase shift between $V_{GS}(t)$ and $I_D(t)$ for different frequencies of $V_{GS}(t)$ is plotted. Except for the instrumental artefact for higher frequencies, the phase shift starts increasing and reaches to around 17° at around 0.4 Hz. The half value of the maximum phase shift is given at 0.13 Hz, which corresponds to a time constant of 1.2 s according to the conventional definition of the delay time. The presence of this intrinsic time constant $\tau_s = 1.2$ s opens an interesting possibility; we can use it to implement a slow-varying threshold dynamics of a kind of artificial neuron as described below.

A typical demonstration of an artificial neuron is to mimic the so-called leaky-integral-and-fire (LIF) functionality, *i.e.*, LIF neuron, using the set-up as shown in Fig. 5(a). The capacitor C_m integrates the input pulses (blue line) arriving from the previous neurons through synapses (both are not shown here), while a resistor R_{leak} slowly discharges C_m. Thus, the gate voltage V_{GS} (and I_D as well) increases (and decreases) as shown in the red line. This process is called "leaky integrate". Then, V_{GS} (I_D as well) eventually reaches to the preset threshold value. The threshold value of I_D is set to trigger an output pulse by using an external circuit, which is not shown in Fig. 5(a). This generation of the output pulse (at the V_{GS} and I_D thresholds) is called "firing". The key factor of LIF is the time constant $\tau_m = R_{leak}C_m$; during the time of τ_m, the next input pulse should reach to the LIF neuron to be integrated.

On the other hand, our STO FET has its intrinsic time constant of τ_s. Input pulses within the time distance τ_s work to decrease the threshold, which is equivalent to the leaky integration. This means our STO FET works as a LIF neuron without the voluminous R_{leak} and C_m. Moreover, the channel is metallic, we can set I_D threshold for firing to be a large value. By this large value of I_D, we can suppress the artefact of the stochastic noises.

We will show a direct implementation of τ_s in our pre-

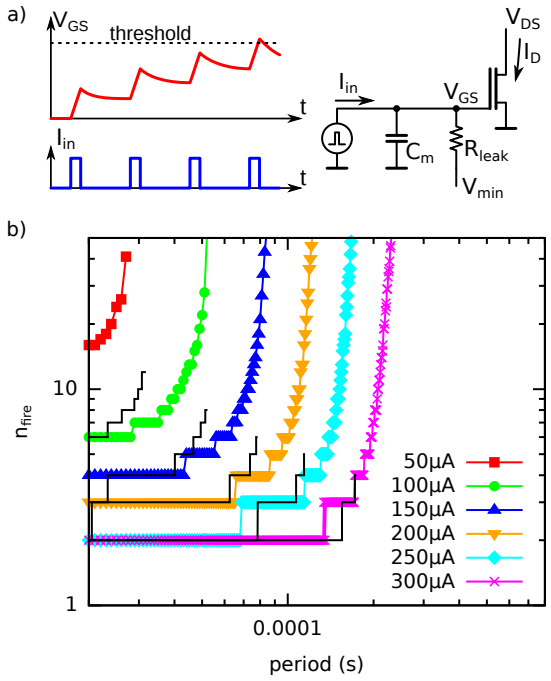

Figure 5: a) Schematic picture of LIF functionality and its set-up. b) Comparison of the standard FET simulation (solid lines) and our STO FET experiments (symbols) for the set-up shown in (a) with $C_m = 1$ nF and $R_{leak} = 10^5\,\Omega$. The width of the input pulses is $10\,\mu$s. See text for details.

sentation, but here we show briefly an implicit evidence of the τ_s effect seen in the standard LIF experiment. Figure 5(b) is a typical plot of LIF functionality exhibiting the number of input pulses required to fire n_{fire} as a function of the period of the pulses for different pulse amplitudes. If we use a standard FET for the transistor in the right panel of Fig. 5(a), we obtain the results shown in black solid lines (the results are obtained by simulations.) For smaller amplitude of the pulse, more number of pulses are required to fire. For longer period of the pulses, more number of pulses are also required, and there exists the longest period, above which the firing never occurs regardless of the number of pulses. These are easily understood by considering the leaky integration with R_{leak} and C_m.

However, if we replace the standard FET to our STO FET, the black solid lines change as shown by the coloured symbols. Because we have two leaky integration effects by τ_m and by τ_s together, smaller number of pulses are enough to fire. Moreover, since $\tau_s = 1.2$ s is almost five orders longer than $\tau_m = R_{leak}C_m = 0.1$ ms, the leaky integration is still effective for longer period of pulses and we could not reach to the limit in our experiment. This indicates the time constant τ_s due to IMT of STO can be used not only for saving the bulky R_{leak} and C_m part but also used for adding another longer and effective time scale to our LIF neuron.

6. Conclusions

The FET fabricated on the STO surface shows IMT when the creation of extrinsic V_O^+ in the channel is suppressed and the electric drift of intrinsic V_O^+ is well-controlled by gating. The sudden change of the screening length gives rise to the large hysteresis and the phase shift (intrinsic time constant) between V_{GS} and I_D. The former is utilised for an artificial synapse and the latter gives a special feature for the device to be used as an artificial neuron. A great advantage is that both synapse and neuron are made of the same material. Furthermore, the device works with the metallic channel containing a large number of carriers, which is beneficial for scaling as well as the large dynamic range to suppress stochastic artefacts.

Acknowledgments

P. S. acknowledges the support of the Spanish Ministry of Economy through the Ramón y Cajal sub-program (RYC-2012-01031). This work was supported by JSPS KAKENHI Grant Numbers 15H02113 (category A) and 15F15315, and by National Institute for Materials Science as the "Nanotechnology Platform" Program of MEXT, Japan.

References

[1] Isao H. Inoue and Hisashi Shima, *Japan Patent* Number 552268, 2014.

[2] N. Kumar, A. Kitoh, I. H. Inoue, *Sci. Rep.*, vol. 6, p. 25789, 2016.

[3] H. Nakamura *et al.*, *Appl. Phys. Lett.* vol. 89, p. 133504, 2006.

[4] A. R. Schulman *et al.*, *Appl. Phys. Lett.*, vol. 110, p. 013502, 2017.

[5] A. B. Eyvazov *et al.*, *Sci. Rep.*, vol. 3, p. 1721, 2013.

[6] H. Nakamura *et al.*, *J. Phys. Soc. Jpn.* vol. 78, p. 083713, 2009.

[7] R. Zazpe *et al.*, *Appl. Phys. Lett.* vol. 103, p. 073114, 2013.

[8] T. Baiatu *et al.*, *J. Am. Cerom. Soc.* vol. 73, p. 1663, 1990; R. Waser *et al.*, *Adv. Mater.* vol. 21, p. 2632, 2009; J. Hanzig *et al.*, *Phys. Rev. B* vol. 88, p. 024104, 2013; B. Khanbabaee *et al.*, *Appl. Phys. Lett.* vol. 109, p. 222901, 2016.

[9] B. Linares-Barranco *et al.*, *Frontiers in Neuroscience* vol. 5, p. 26, 2011.

[10] S. H. Jo *et al.*, *Nano letters* vol. 10, pp. 1297-1301, 2010.